High energy resolution $CsPbBr_3$ alpha particle detector with a full-customized readout application specific integrated circuit

Xin Zhang[1,2], Ruichen Bai[1,2], Yuhao Fu[3], Yingying Hao[1,2], Xinkai Peng[1,2], Jia Wang[2,3*], Bangzhi Ge[1,2], Jianxi Liu[1], Yongcai Hu[2,4], Xiaoping Ouyang[5*], Wanqi Jie[1,2], Yadong Xu[1,2*]

[1]School of Materials Science and Engineering, Northwestern Polytechnical University, Xi'an 710072, PR China

[2]Key Laboratory of Radiation Detection Materials and Devices, Ministry of Industry and Information Technology, Xi'an 710072, PR China

[3]School of Electronics and Information, Northwestern Polytechnical University, Xi'an 710072, PR China

[4]School of Computer Science, Northwestern Polytechnical University, Xi'an 710072, PR China

[5]Northwest Institute of Nuclear Technology, Xi'an 710024, PR China

*E-mail: jwang@nwpu.edu.cn (J. Wang); oyxp2003@aliyun.com (X. Ouyang); xyd220@nwpu.edu.cn (Y. Xu).

Table of contents

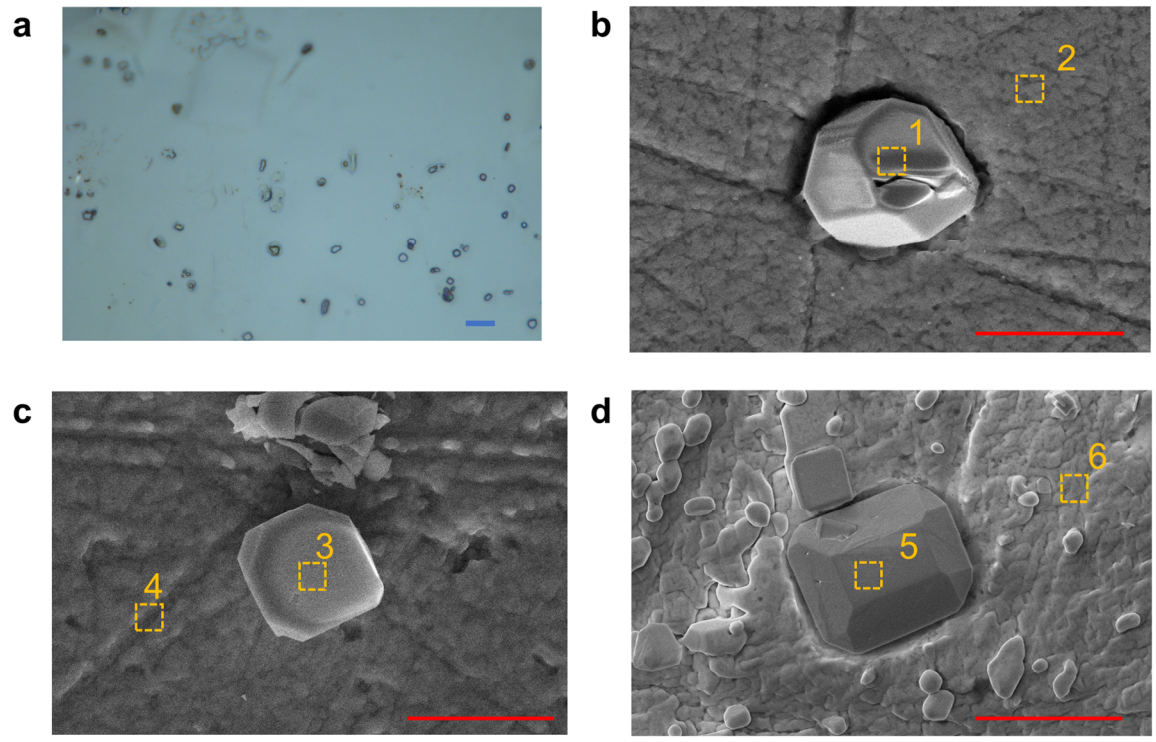

Supplementary Fig. 1 Characterization of $CsPb_2Br_5$ defects. (a) The optical microscope image. The scale bar in blue color is 10 μm. (b)-(d) Typical SEM images of $CsPb_2Br_5$ phases particles with regular polyhedral morphology. The scale bars in red color are 5 μm. The EDS results represented by the yellow squares are shown in the supplementary table1.

Supplementary Table 1 The atomic percentage of the elements at different sites measured by EDS micro-area test.

Elements	1	2	3	4	5	6
Cs	12.23 %	21.25 %	13.10 %	20.18 %	12.48 %	20.12%
Pb	25.97 %	19.12 %	24.62 %	19.99 %	26.69 %	19.78 %
Br	61.79 %	59.62 %	62.28 %	59.83 %	60.33 %	60.10 %
Total	100 %	100 %	100 %	100 %	100 %	100 %

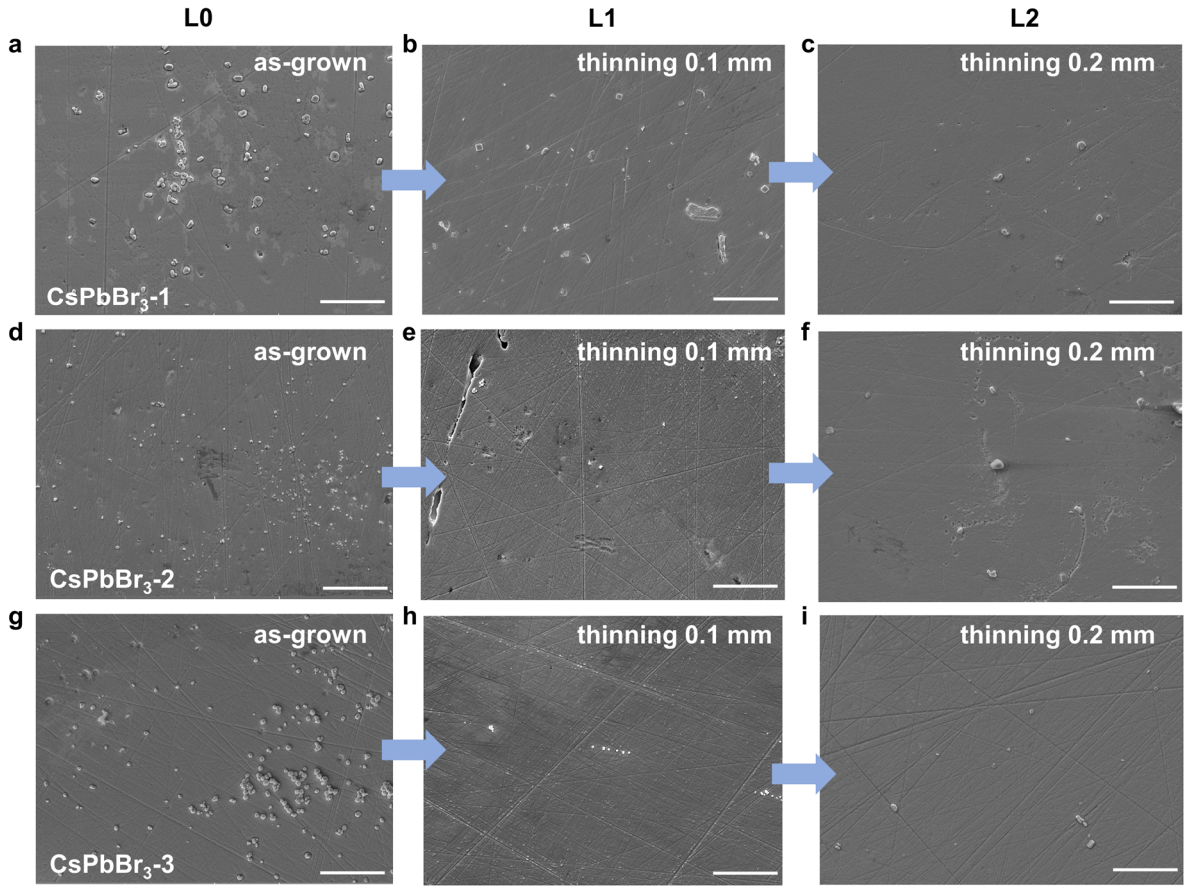

Supplementary Fig. 2 The typical SEM images of spatial inhomogeneous distribution of the $CsPbBr_3$ surface along the vertical thickness of the $CsPbBr_3$ crystal. (a) $CsPbBr_3$-1 before and (b) (c) after thinning. (d) $CsPbBr_3$-2 before and (e) (f) after thinning. (g) $CsPbBr_3$-3 before and (h) (i) after thinning. All scale bars in white color are 50 μm.

Supplementary Table 2 The proportion of $CsPb_2Br_5$ before and after thinning.

	L0	L1	L2
$CsPbBr_3$-1	24.8%	11.4%	5.1%
$CsPbBr_3$-2	7.5%	3.9%	1.7%
$CsPbBr_3$-3	9.2%	4.2%	1.1%

Here, we define the proportion of $CsPb_2Br_5$ defects as the fractional area occupied according to the SEM images.

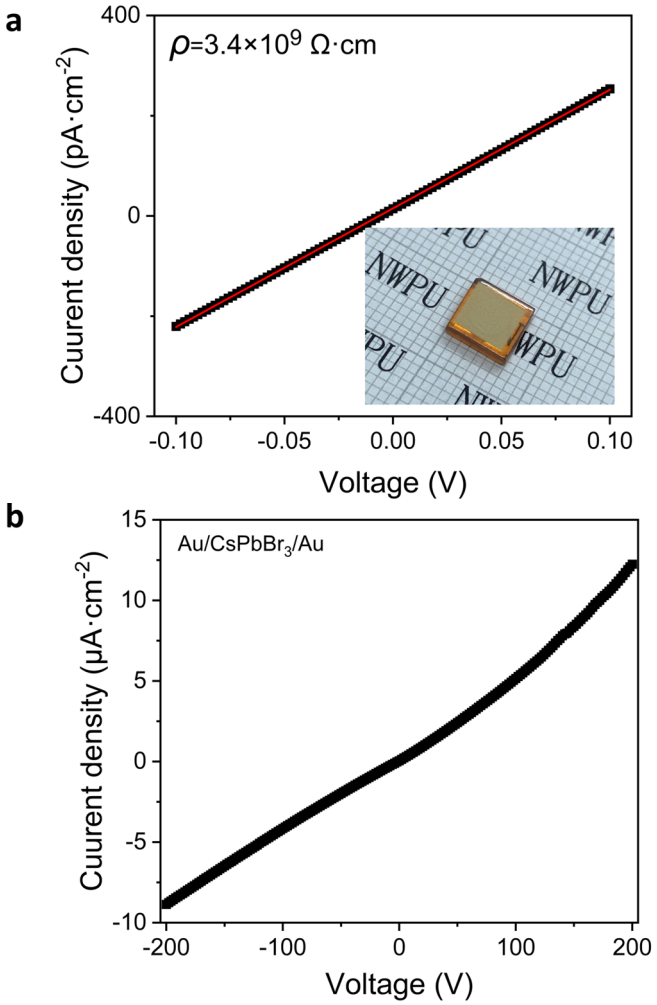

Supplementary Fig. 3 The typical *J-V* curves of the Au/CsPbBr3/Au device. Ranging from (a) -0.1 V to 0.1 V and (b) -200 V to 200 V. Inset: the Au/CsPbBr3/Au detector.

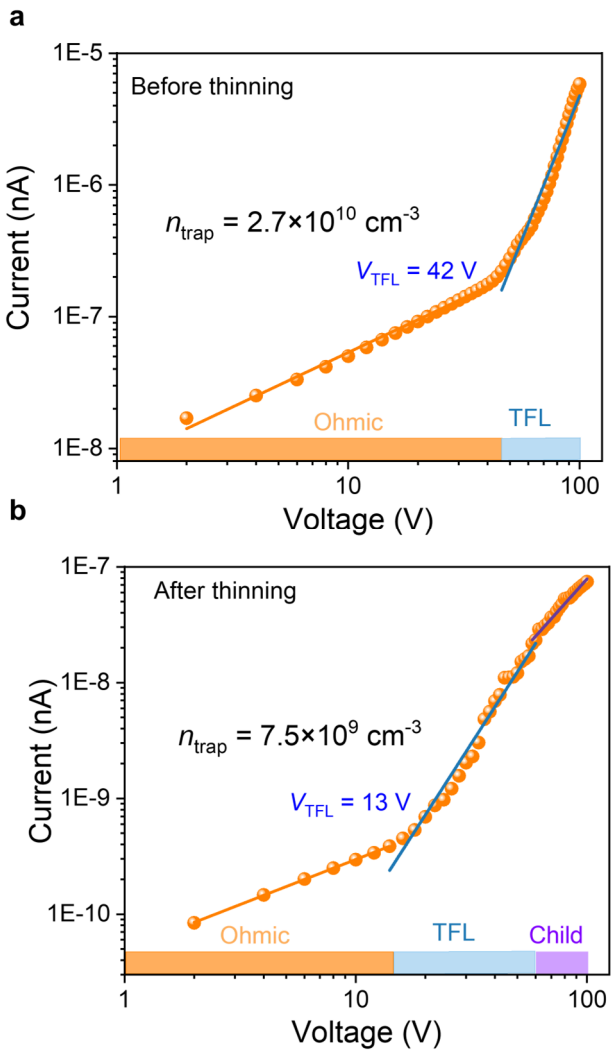

Supplementary Fig. 4 Current-voltage curves of $CsPbBr_3$. (a) Before and (b) after thinning.

The space-charge-limited-current (SCLC) is a technique that has been widely employed for determining the charge carrier mobility. In SCLC measurements, there are three transition regimes: Ohmic, trap-filled limited (TFL), and child[3, 4]. The trap state densities were calculated as:

$$n_{\text{trap}=} \frac{2\varepsilon_0 \varepsilon_r V_{\text{TFL}}}{qd^2} \quad (1)$$

where V_{TFL} is the trap-filled limit voltage, d is the detector thickness, ε_0 is the vacuum permittivity, ε_r is the relative dielectric constant for $CsPbBr_3$, q is the electric quality, n_{trap} is trap density.

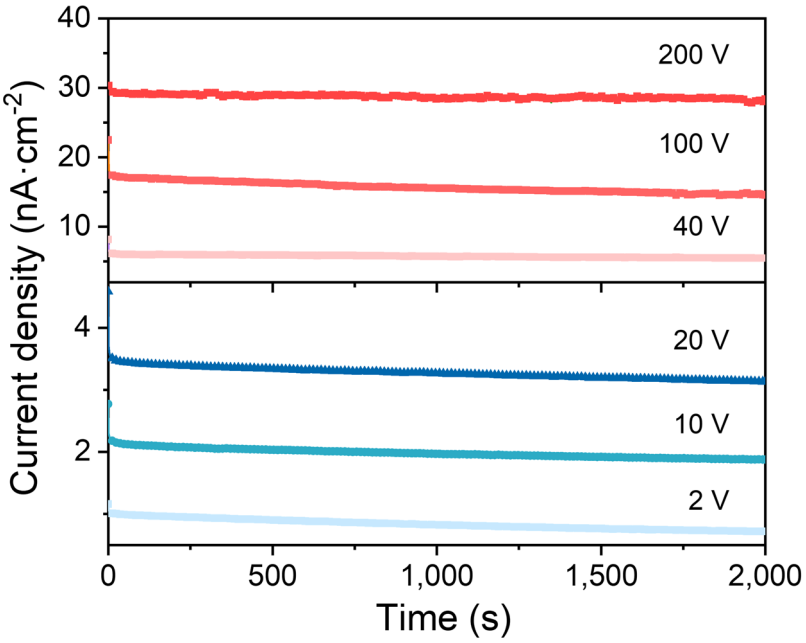

Supplementary Fig. 5 Current as a function of time at different biases. Voltage from 2 V to 200 V.

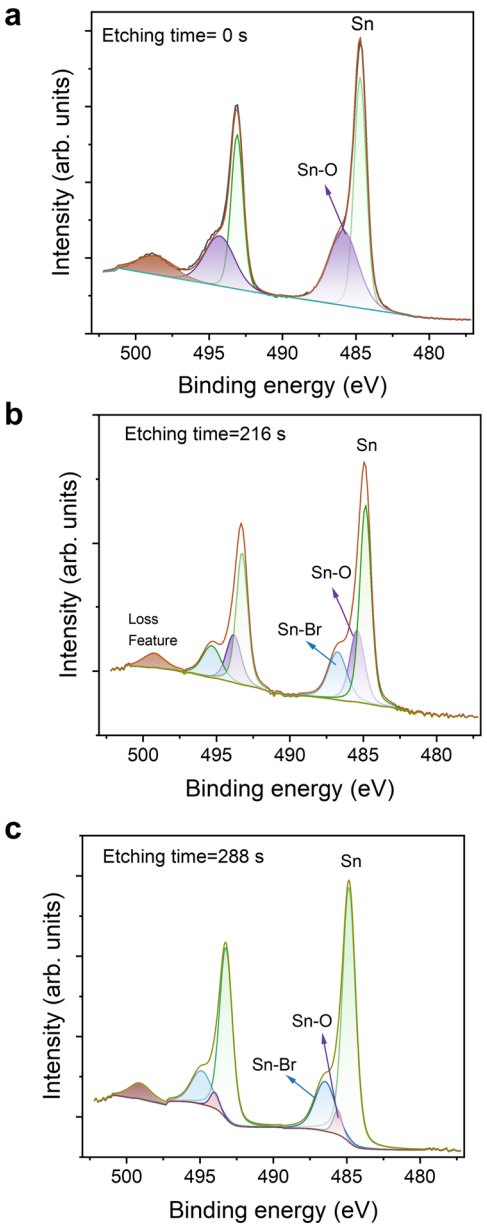

Supplementary Fig. 6 X-ray photoelectron spectroscopy (XPS) measurements with different eating time. (a) 0 s. (b) 216 s. (c) 288 s.

According to XPS results, the chemical states of Sn can be attributed to metallic and ionic states, as shown in Supplementary Fig. 6. The peak at 485.6 eV attributed to the oxidation of Sn, and the peaks at 486.7 eV attributed to the formation of Sn-Br compound. With the increase in etching depth, the proportion of Sn-Br gradually increases, while the proportion of Sn-O decreases gradually.

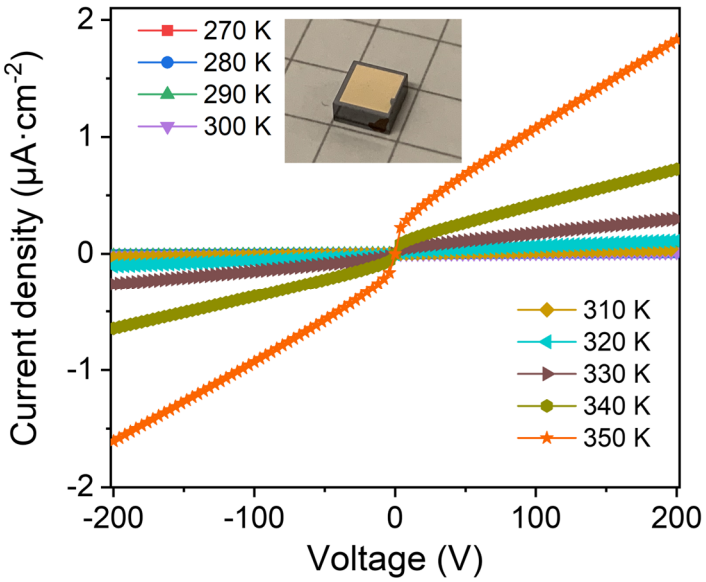

Supplementary Fig. 7 Temperature dependence response of the CdZnTe device from 270 K to 350 K (thickness is 2 mm, electric filed is 1,000 V·cm^{-1}). Inset: the Au/CdZnTe/Au detector.

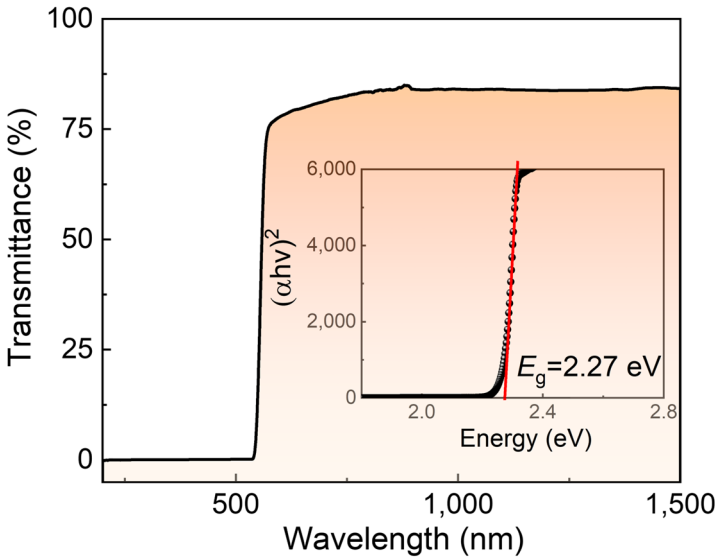

Supplementary Fig. 8 The optical diffuse reflectance spectra of $CsPbBr_3$. The inset is the absorbance spectra derived using the Kubelka-Munk function.

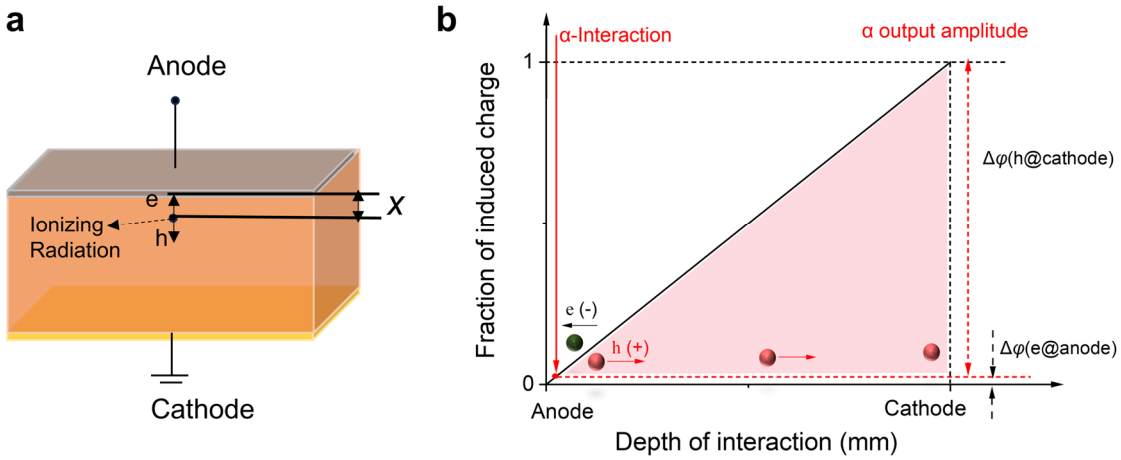

Supplementary Fig. 9 Depth dependent charge sensing. (a) Detector with planar electrodes (b) Signal contributions from holes and electrons in an ideal detector. Δφ(e@anode) and Δφ(h@cathode) represents the change in the weighting potential at the anode and the cathode, respectively.

In 1938, Shockley[5] and Ramo[6] calculated the Shockley-Ramo principle, *i.e.*, in a parallel-plate capacitor with 1 V applied to one electrode and the other electrode grounded, the light enters the carriers formed at a depth of x, as shown in Supplementary Fig. 9. The induced charge generated on the detector pole plate when the carriers move satisfies:

$$Q(x)=\frac{q}{d}\left\{\int_0^x N_{\mathrm{e}}(x)dx_{\mathrm{e}}+\int_x^x N_{\mathrm{h}}(x)dx_{\mathrm{h}}\right\} \tag{2}$$

where x is the position from the electrode that the ionizing radiation is incident on, d is the thickness, q is electric quantity. Assuming that the capture centers are uniformly distributed in the crystal and that the carrier transport lifetime is sufficiently long, the number of carriers are:

$$N_{\mathrm{e}}(x)=N_0\exp(-\frac{x}{(\mu\tau)_{\mathrm{e}}E}) \tag{3}$$

$$N_{\mathrm{h}}(x)=N_0\exp(-\frac{d-x}{(\mu\tau)_{\mathrm{h}}E}) \tag{4}$$

Where N_0 is the initial number of the electron-hole pairs, and the $\mu\tau$ product for holes (h) and electrons (e) are specified. The ratio of the induced charge to the initial charge Q_0 is defined as

the charge collection efficiency η (Charge Collection Efficiency, CCE):

$$\eta = \frac{Q(x)}{Q_0} = \frac{(\mu\tau)_e}{d}(1-\exp(\frac{-x}{(\mu\tau)_e E})) + \frac{(\mu\tau)_h}{d}(1-\exp(\frac{x-d}{(\mu\tau)_h E})) \quad (5)$$

The contribution of electrons to charge can be ignored when the radiation source is incident from the anode electrode due to the depth of incidence of alpha particles is only a few tens of um (Supplementary Fig. 9b). Therefore, the CCE for the α-particle induced pulse height spectrum of the p-type perovskite detector is calculated using the Hecht equation[7]:

$$\eta = \frac{\mu\tau E}{d}(1-\exp(\frac{-d}{\mu\tau E})) \quad (6)$$

It is worthy noticing that the Hecht equation is applicable when the electrical field and traps are distributed uniformly thorough out the detector.

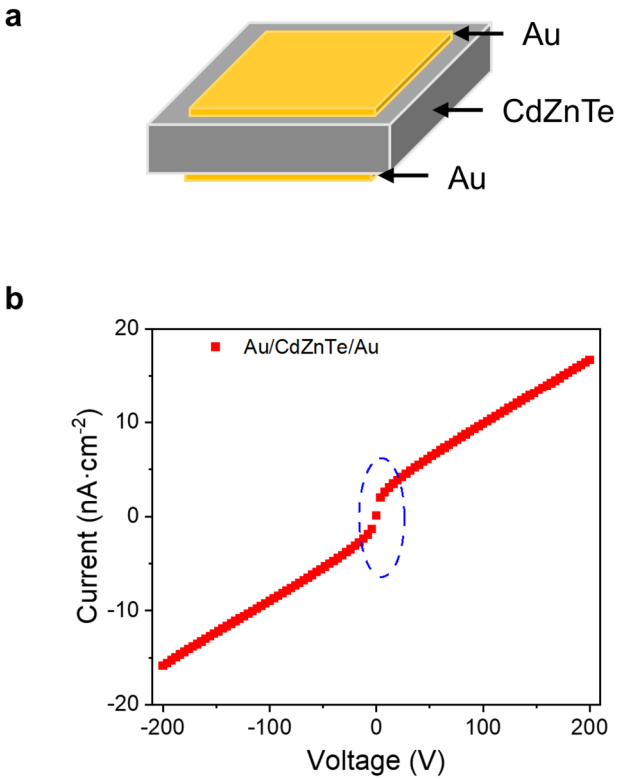

Supplementary Fig. 10 The performance of CdZnTe detector. (a) Diagram of Au electrode. (b) The typical *J-V* curves from -200 V to 200 V (thickness is 2 mm).

The work functions of CdZnTe and Au are 4.3 eV and 4.7 eV, respectively. And the interface barrier height was determined to be 1.17 eV for Au-CdZnTe with passivation[8, 9]. Therefore, the Au/CdZnTe contact is a Schottky type[10]. The current curve also shows that the Au/CdZnTe contact is a Schottky contact (Supplementary Fig. 10). Another great feature of the Au/CdZnTe/Au detector is that the Au electrode serves as the charge collection contact, which can also be beneficial in fabricating detectors with pixel or coplanar-grid detectors from the current CdZnTe technology[11]. Moreover, both the Schottky-type Sn/$CsPbBr_3$/Au and the double Schottky type Au/CdZnTe/Au detectors are in reverse bias during operation. Therefore, the Schottky Au/CdZnTe/Au and Au/$CsPbBr_3$/Sn detector are used to compare the dark current.

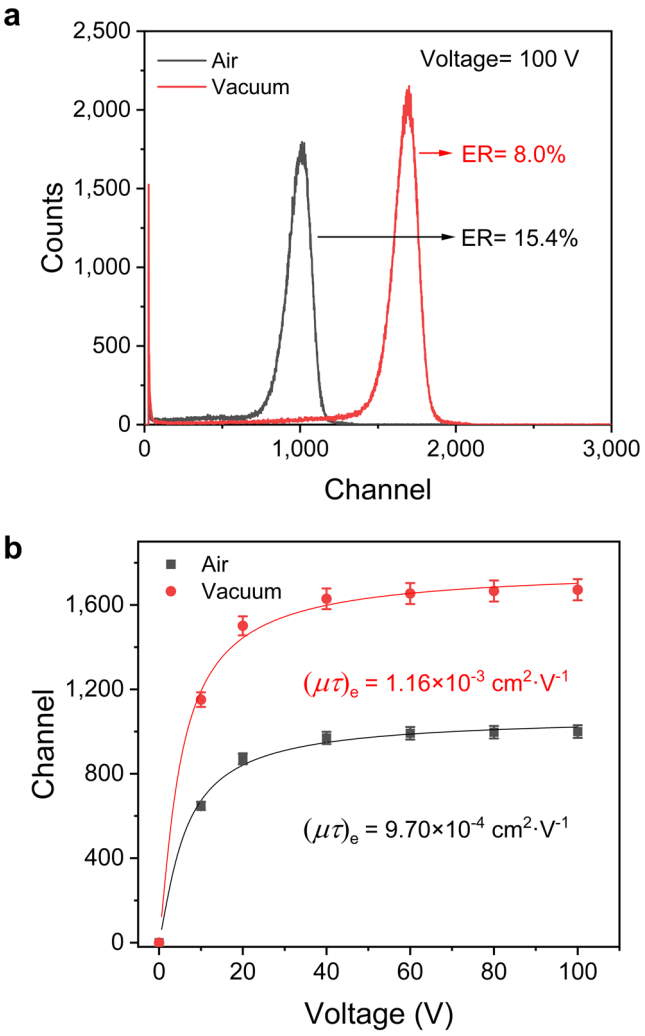

Supplementary Fig. 11 The energy spectra of Au/CdZnTe/Au device in air and vacuum. (a) The energy spectra in air and vacuum. (b) The peak position as a function of bias voltage fit by the Hecht equation. The error bars represent 3% errors.

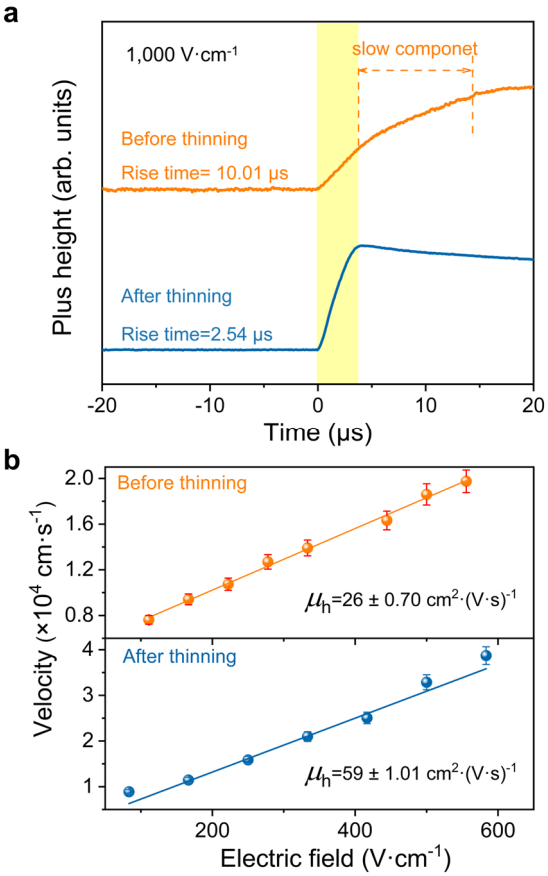

Supplementary Fig. 12 The impact of before and after polishing and thinning on carrier transport performance of $CsPbBr_3$ detector. (a) α particle induced pulse shapes and the rise time under the same electric field strength (1,000 $V \cdot cm^{-1}$). (b) Carrier mobility. The error bars represent 5% errors.

The existence of high-density extended defects enriched in the incoherent interface surrounding $CsPb_2Br_5$ phases tends to act as trapped centers, ultimately affecting the charge carrier drift time and carrier mobility. Moreover, the interfaces between the $CsPb_2Br_5$ defects and the overall spatially heterogeneous 3D distribution of the substrate in the sample destroy the lattice periodicity, build up the barrier for charge carrier transport and form channels for ion migration[12]. Therefore, the existence of $CsPb_2Br_5$ phases increases the carrier transport time and reduces the carrier mobility of the detector.

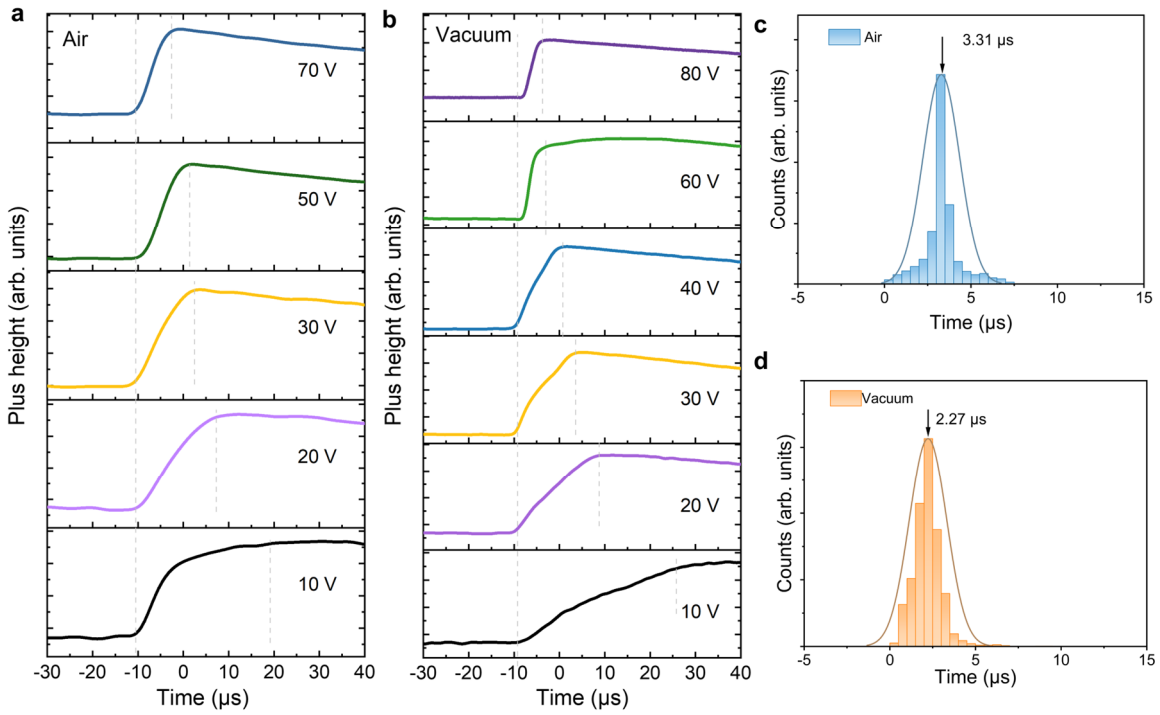

Supplementary Fig. 13 The rise time of $CsPbBr_3$ detector with different applied voltage. (a) Air. (b) vacuum. The distributions of the rise time at 100 V in (c) air and (d) vacuum.

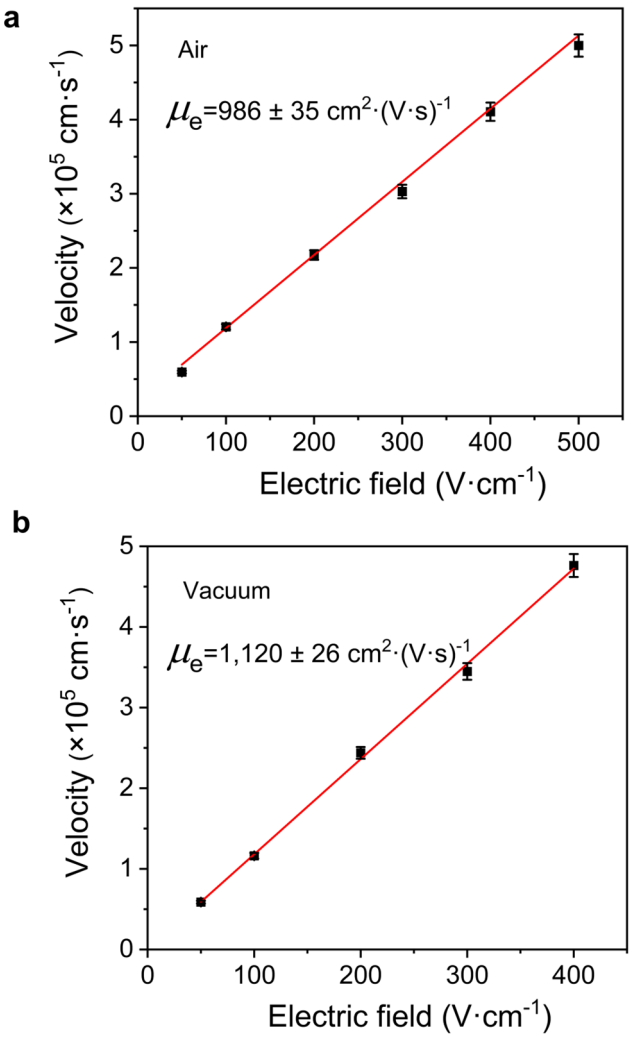

Supplementary Fig. 14 The electrons drifting velocities of CdZnTe detector vs. electric field. (a) Air and (b) vacuum. The error bars represent 3% errors.

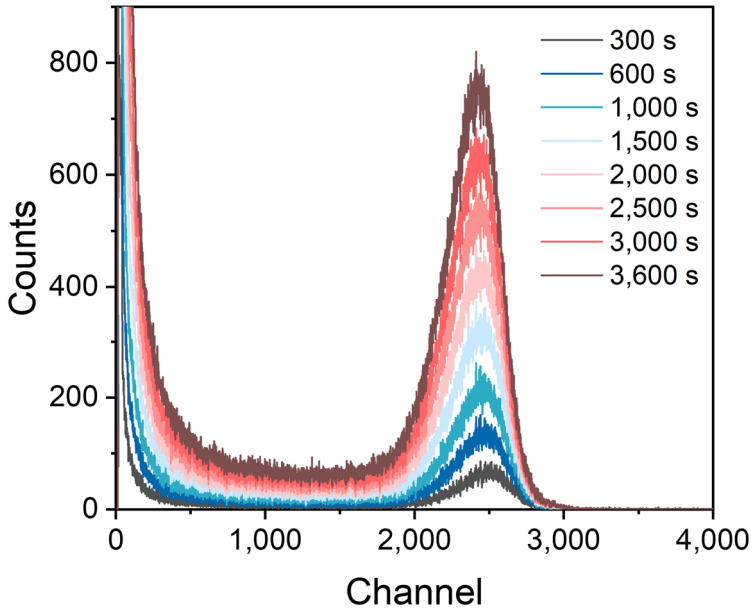

Supplementary Fig. 15 Spectra with different collection time (1,000 V·cm^{-1}).

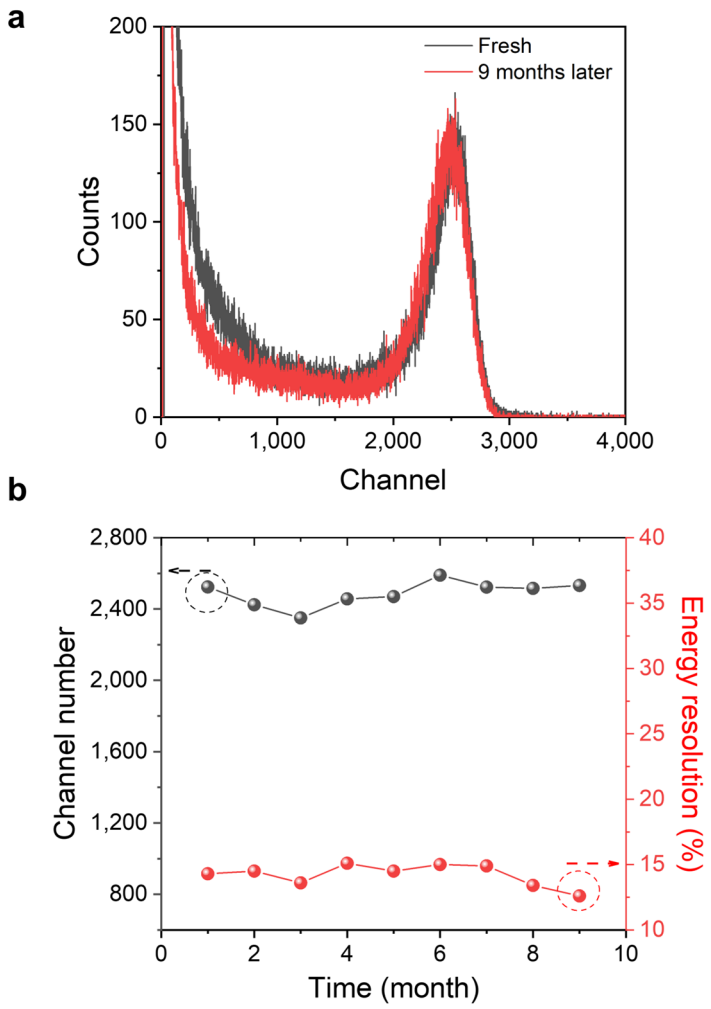

Supplementary Fig. 16 Storage stability of Au/CsPbBr$_3$/Sn detector. (a) Spectrum collected at air for the fresh device and after nine months of storage. (b) The channel number and energy resolution from the testing spectrum biased at 1,000 V·cm^{-1} for nine months.

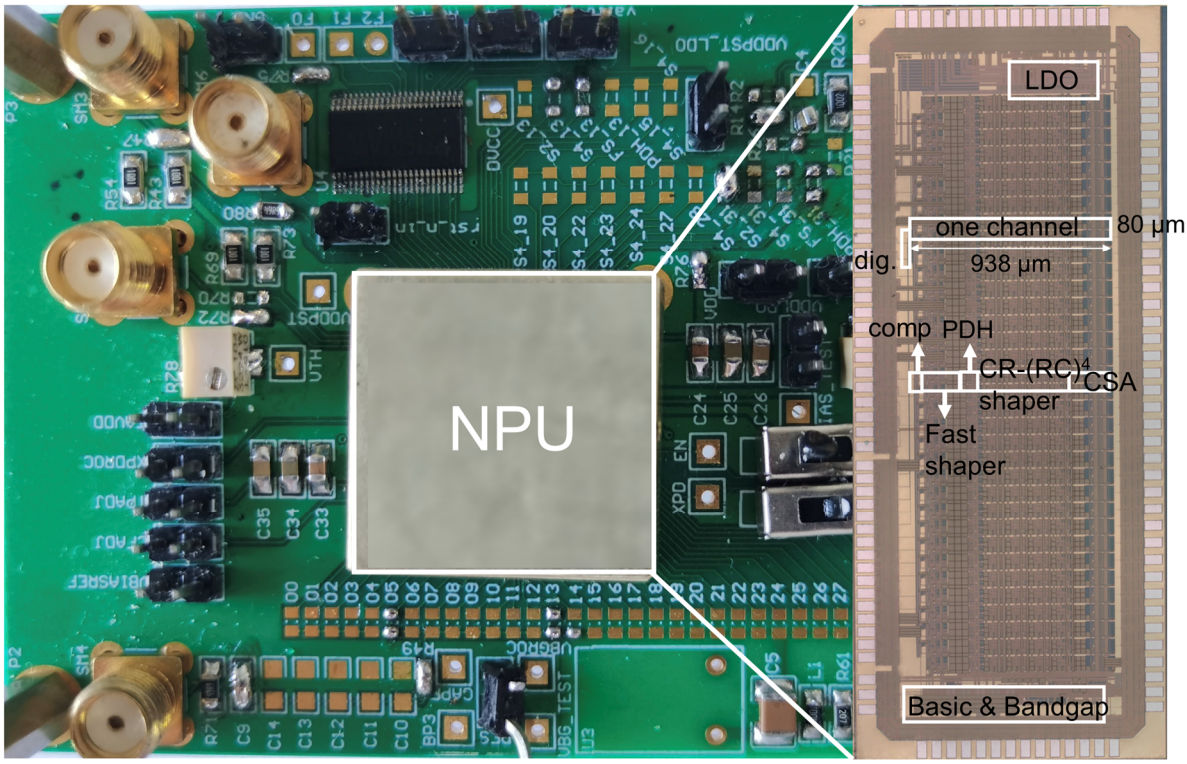

Supplementary Fig. 17 Ultimate chip micrograph and the photo of the measuring board. LDO is a low drop-out regulator. PDH is peak detection and hold. CSA is a charge sensitive amplifier, comp is a comparator, dig. is digital. The CR-$(RC)^4$ shaper is used to amplify and filter the output of CSA.

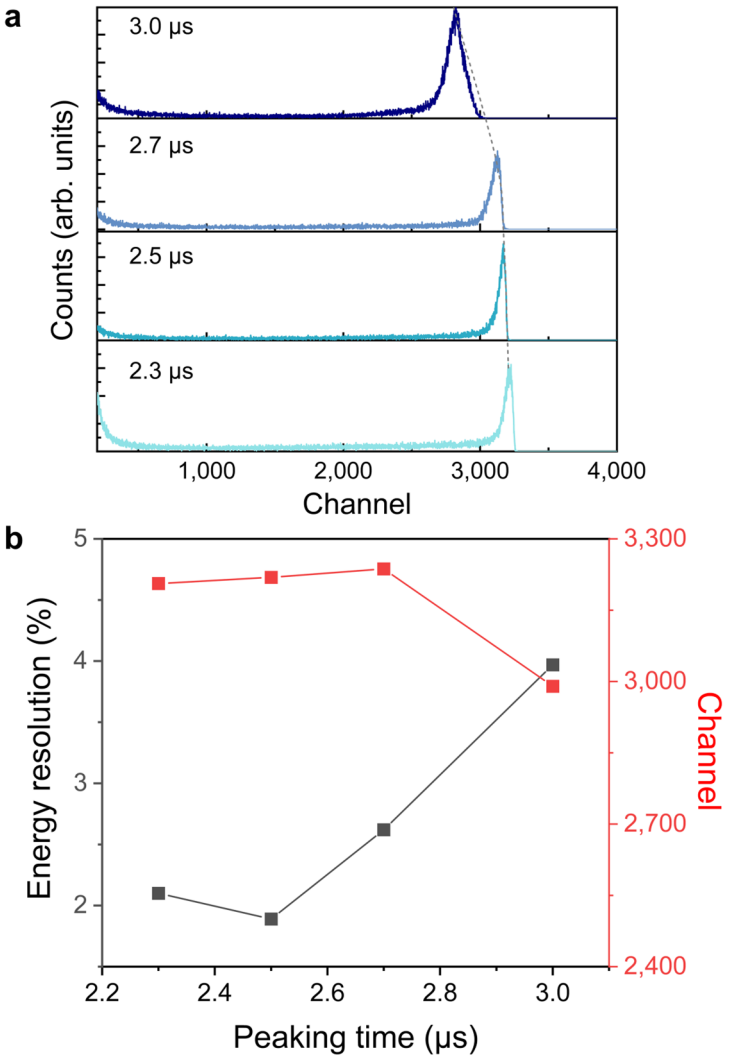

Supplementary Fig. 18 The resulting energy spectra. (a) Different shaping time. (b) The energy resolution and peak channel with different shaping time.

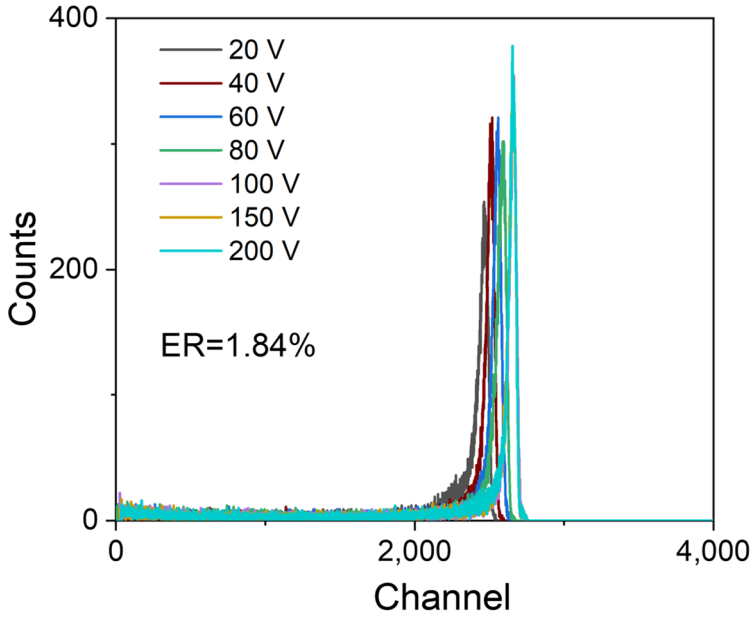

Supplementary Fig. 19 The resulting energy spectra of CdZnTe detector with optimized electronics (thickness is 1 mm).

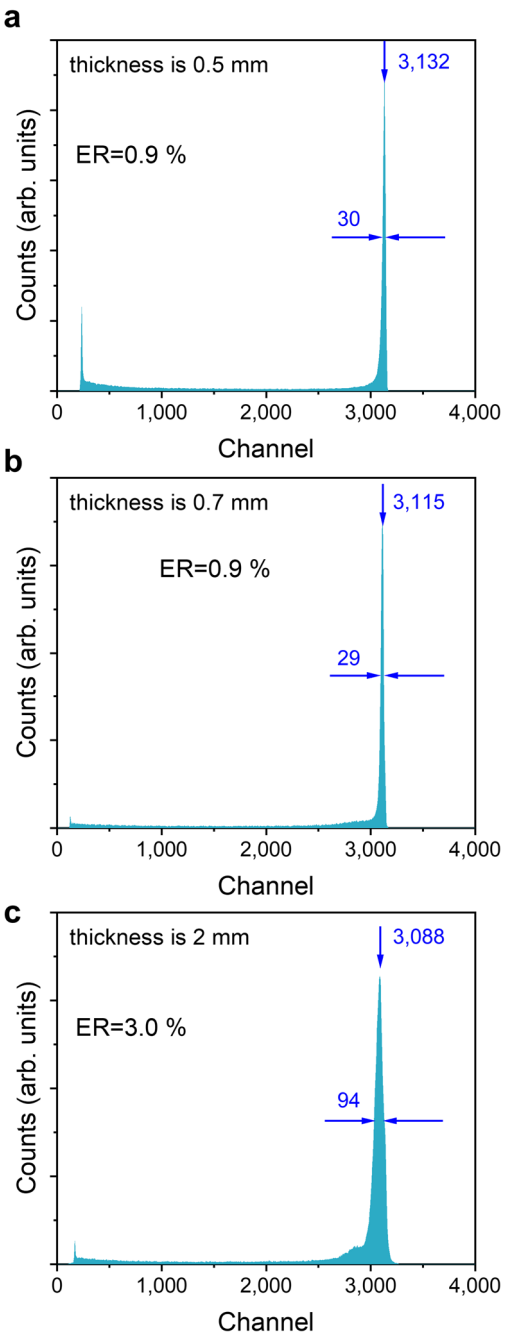

Supplementary Fig. 20 The alpha particle spectra of $CsPbBr_3$ detector with different thicknesses. (a) 0.5 mm, (b) 0.7 mm, (c) 2.0 mm.

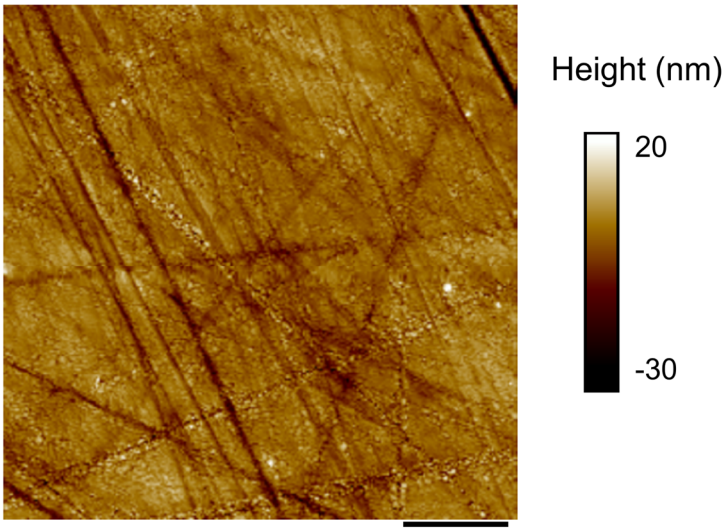

Supplementary Fig. 21 AFM images of wafer surface after surface process. The scale bar in black color is 2 μm.

Supplementary Note

Statistical Limit to Energy Resolution

The expected average number of ion pairs n_0 produced (assuming Fano=0.1[1, 2]):

$$n_0 = \frac{W}{E} = \frac{5.5\times10^6 \text{ eV}}{5.97 \text{ eV}} = 9.21\times10^5 \tag{7}$$

Where E is the energy of α particle, W is ionization energy.

The variance $\sigma_{n_0}^2$ in this number is given by:

$$\sigma_{n_0}^2 = Fn_0 = 0.1\times9.21\times10^5 = 9.21\times10^4 \tag{8}$$

The standard deviation σ_{n_0}:

$$\sigma_{n_0} = \sqrt{Fn_0} = 303 \tag{9}$$

For the expected Gaussian distribution describing n_0, the full-width-at-half-maximum (FWHM) is just the shape factor of 2.35 multiplied by σ, leading to:

$$\text{FWHM}(n_0) = 2.35\sigma = 712 \tag{10}$$

The FWHM in units of particle energy is:

$$\text{FWHM}(E) = 2.35\sigma\cdot W = 4.25 \text{ keV} \tag{11}$$

The energy resolution (ER) of statistical limit:

$$\text{ER} = \frac{\text{FWHM}(E)}{E} = 0.077\% \tag{12}$$

Supplementary References

1. He, Y. et al. $CsPbBr_3$ perovskite detectors with 1.4% energy resolution for high-energy γ-rays. *Nat. Photon*. **15**, 36-42 (2020).
2. Harrison, M. J., McGregor, D. S., Doty, F. P., Fano factor and nonuniformities affecting charge transport in semiconductors. *Physical Review B* **77**, 195207 (2008).
3. Zhang, Z. et al. Charge carrier mobilit y of halide perovskite single crystals for ionizing radiation detection. *A*ppl. P*hys. Lett.* **119**, 030502 (2021).
4. Garcia-Batlle, M. et al. Coupling between ion drift and kinetics of electronic current transients in $MAPbBr_3$ single crystals. *ACS Energy Lett.* **7**, 946-951 (2022).
5. Shockley, W., Currents to conductors induced by a moving point charge. *J. Appl. Phys.* **9**, 635-636 (1938).
6. Ramo, S., Currents Induced by Electron Motion. *Proceedings of the IRE* **27**, 584-585 (1939).
7. Hecht, K., Zum Mechanismus des lichtelektrischen Primrstromes in isolierenden Kristallen. *Z. Physik* **77**, 235-245 (1932).
8. Prokesch, M.; Szeles, C., Accurate measurement of electrical bulk resistivity and surface leakage of CdZnTe radiation detector crystals. *J. Appl. Phys.* **100**, 014503 (2006).
9. Li, Q. et al., Investigation on interface barrier of Au-CdZnTe contacts. *Nucl. Instrum. Meth. A* **564**, 544-548 (2006).
10. Yang, F et al., A modified diffusion model for characterization of real I-V curve and charge collection efficiency of CdZnTe detectors. *Nucl. Instrum. Meth.* **959**, 163515 (2020).
11. Yang, G. et al., Performance of common-grid pixelated CZT detector with different array geometries. *J. Instrum.* **10** , P06008-P06008 (2015).
12. Li, M. et al., Synthesis of two-dimensional $CsPb_2X_5$ (X = Br and I) with a stable structure and tunable bandgap by $CsPbX_3$ phase separation. *J. Phys. Chem.Lett.* **13**, 2555-2562 (2022).